Breaking FOV-Aperture Trade-Off With Multi-Mode Nano-Photonic Antennas

Reza Fatemi, *Student Member, IEEE*, Parham P. Khial, *Student Member, IEEE*, Aroutin Khachaturian, *Student Member, IEEE*, and Ali Hajimiri, *Fellow, IEEE*

(Invited Paper)

***Abstract*—Nano-photonic antennas are one of the key components in integrated photonic transmitter and receiver systems. Conventionally, grating couplers, designed to couple into an optical fiber, suffering from limitations such as large footprint and small field-of-view (FOV) have been used as on-chip antennas. The challenge of the antenna design is more pronounced for the receiver systems, where both the collected power by the antenna and its FOV often need to be maximized. While some novel solutions have been demonstrated recently, identifying fundamental limits and trade-offs in nano-photonic antenna design is essential for devising compact antenna structures with improved performance. In this paper, the fundamental electromagnetic limits, as well as fabrication imposed constraints on improving antenna effective aperture and FOV are studied, and approximated performance upper limits are derived and quantified. By deviating from the conventional assumptions leading to these limits, high-performance multi-mode antenna structures with performance characteristics beyond the conventional perceived limits are demonstrated. Finally, the application of a pillar multi-mode antenna in a dense array is discussed, an antenna array with more than 95% collection efficiency and 170° FOV is demonstrated, and a coherent receiving system utilizing such an aperture is presented.**

***Index Terms*—Phased arrays, nanotechnology, antenna arrays, antenna efficiency, antenna gain, antenna radiation patterns, antenna theory, antennas, aperture efficiency, optical arrays.**

I. Introduction

AN INTEGRATED nano-photonic antenna is a planar structure fabricated on a chip [1]–[17] which is defined as a transducer that couples the guided mode into the free-space mode and vice versa[1] [4]. In other words, an antenna is an on-chip component that in the transmitter setting is fed with a guided mode and radiates into the free-space, and in the receiver setting, captures the free-space incident wave and couples it into a waveguide (Fig. 1). Nano-photonic antennas have application in many recently demonstrated integrated photonic systems such as optical phased array transmitters [1]–[4], [18], [19] and receivers [7], [12], nano-photonic coherent imager [13], wireless optical communication [14], lens-less cameras [16], [17], etc. For implementing most of today's low cost, high-yield, and commercial systems, silicon photonic integration technology with a single photonic layer of silicon is used [4]. A silicon photonic platform is often realized on a silicon-on-insulator (SOI) process (Fig. 1) in which the top silicon layer is used to realize photonic components, including antennas, through etching and patterning. Moreover, various etching levels, doping layers, and metal layers are provided to realize photonic components and interfacing, as well as germanium layer for photo-detection in some near-infrared wavelengths. Moreover, to achieve low loss and visible range photonic components, silicon nitride has been used as the photonic layer material in some platforms [19].

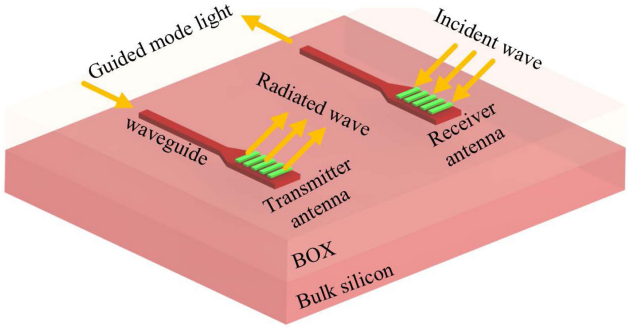

Fig. 1. Schematic of a standard SOI silicon photonic platform consisting a bulk silicon substrate and a buried oxide layer (BOX). Optical components including transmitter and receiver nano-photonic antennas are fabricated by patterning the silicon layer on the BOX.

In the early implementations of integrated photonic systems, conventional grating couplers were used as transmitter antennas [1], [2], [13]–[15], [19]. However, the large footprint of a grating coupler is a limiting factor in many systems such as dense antenna arrays. Moreover, the need to selectively/collectively improve specifications of the antennas such as field-of-view (the angular range that the antenna is an effective radiator/receiver), radiation efficiency (the fraction of power coupled to free-space), and form factor has recently motivated the researchers to devise novel antenna topologies with improved performance. Deviating from grating structures allows achieving higher radiation efficiency [4]. Moreover, an ultra-compact broadband antenna is

Manuscript received May 28, 2020; revised July 24, 2020 and September 15, 2020; accepted September 16, 2020. Date of publication September 25, 2020; date of current version October 15, 2020. *(Corresponding author: Reza Fatemi.)*

The authors are with the Department of Electrical Engineering, California Institute of Technology, Pasadena, CA 91125 USA (e-mail: sfatemi@caltech.edu; pporsand@caltech.edu; akhachat@caltech.edu; hajimiri@caltech.edu).

Color versions of one or more of the figures in this article are available online at https://ieeexplore.ieee.org.

Digital Object Identifier 10.1109/JSTQE.2020.3026966

[1]This is the same definition used for conventional microwave antennas

realized via optimization of the silicon slab etching pattern [18]. In addition to devising novel antenna structures on a single photonic layer process, by adding a high contrast grating on top of the antenna structure [8] and bottom reflectors [6], [10] the radiation efficiency of the antenna is improved significantly. However, most of these works are limited to antennas with large footprints which often have an FOV that is narrow in one of the dimensions.

In addition to the transmitter antenna, a photonic receiver system [7], [13], [16], [20] also incorporates antennas that collect the incident power and output to waveguides. The waveguides are then used to route the optical signals for further processing. Since the received signal is weak in many applications, for a given physical size of the antenna, the largest effective aperture is desired to maximize the signal-to-noise ratio, sensitivity of the system, and robustness to noise. While techniques such as heterodyne detection [7] can be used to increase the sensitivity of the system, a larger collection area is always beneficial to a receiver system and allows for operation at lower received signal levels and noisier environments. Moreover, the FOV of the antenna needs to be in harmony with the FOV of the system. A limited antenna FOV directly affects the performance of the system. For instance, in an optical phased array, small antenna FOV translates to a limited steering range. Conventional photonic antenna structures impose a compromise between FOV and effective aperture, i.e., a standard antenna with a large effective aperture is limited in the angular range that it can operate and vice versa.

In this paper, we study the performance characteristics of nano-photonic antennas from the transmitter antenna perspective, derive approximate performance bounds for antenna design in standard single-layer silicon photonic processes, and provide solutions to reach/approach the conventional limits. Furthermore, the inter-dependency of the antenna specifications in the transmitter and the receiver settings are illustrated and quantified. Using these relationships, design pathways for realizing high-performance receiver antennas are discussed and multiple receiver antenna structures that can break the fundamental trade-off between the effective aperture and FOV are demonstrated. Moreover, the application of a presented multi-mode antenna in a dense-array coherent receiver system is demonstrated.

II. Receiving Photonic Antenna

A single-port receiving antenna couples the impinging light into a guided mode within an on-chip planar waveguide. Its effective aperture is defined as

$$A(\theta,\phi) = P_o/S_i, \tag{1}$$

where P_o is the total power coupled into the waveguide attached to the antenna port and S_i is the power density (defined by Poynting vector) of a plane wave arriving from the direction defined by (θ,ϕ), assuming they are polarization matched. If the polarization state of the incident light, on the Poincare sphere representation, deviates from the polarization that results in the maximum power collection by an angle ψ, a polarization matching factor of $\cos^2(\psi/2)$ must be added to the above equation [21], which can reduce the effective aperture (down to zero) for a mismatched polarization. Hence, the ability to couple into both polarizations is a desirable feature of any design. Whenever there is a need for high signal strength and a large signal-to-noise ratio (almost always), a high effective aperture is desirable. Effective aperture as a function of θ and ϕ defines the receiving pattern of the antenna. For any given application, a minimum FOV must be achieved, while maximizing the collection area.

Increasing the effective aperture faces limitations in different applications. For instance, in an optical phased array, if the individual element antenna size is increased to collect more power, the element spacing needs to be increased accordingly to fit the antennas. Increasing the element spacing reduces the grating lobe spacing in the array pattern, which can limit the effective grating-lobe-free beam steering range (FOV) of the optical phased array [4]. Moreover, by conservation of energy, the effective aperture of each antenna in a large array cannot exceed the unit grid area, defined by the array pitch. If an array is made of individual elements whose standalone effective aperture exceeds this limit, the effective aperture within the array will be reduced through coupling with adjacent elements.

On the other hand, in the transmitter setting, it is desired to maximize the radiation efficiency of the antenna which is defined as the ratio of the total power radiated by an antenna to the net power fed into it.[2] The radiated power is desired to be distributed on a certain angular range or FOV which is a property of the antenna pattern. Antenna pattern or directivity pattern, $D(\theta,\phi)$, is a function of elevation angle, θ, and azimuth angle, ϕ, and characterizes the relative power density in each direction to the average power density radiated by the antenna.[3]

There is a well-known antenna reciprocity relationship between the receive and transmit patterns of a single-port antenna that imposes a trade-off between its FOV and effective aperture. We will present a short derivation of this reciprocity and use the setting in the subsequent sections for additional discussions of the FOV and effective aperture trade-offs.

Consider the setting of Fig. 2, with the antenna under test (AUT) and a measurement antenna (MA) at a very large distance R at (θ,ϕ) (shown at two different locations in the figure). MA is oriented such that it is polarization matched to the AUT. Both antennas have a single-mode port. Thus, a two-port network model with a scattering matrix of $\mathbf{S}$ is sufficient to analytically represent the system. The parameters of the scattering matrix depend on the location of the MA and are functions of (θ,ϕ). When AUT is in the transmit mode, the antenna pattern (directivity) of AUT can be measured by sweeping MA over (θ,ϕ). The power transfer from AUT to MA is given by $|s_{21}(\theta,\phi)|^2$ at each (θ,ϕ). Therefore, the directivity of the antenna is proportional to

$$D(\theta,\phi) \propto \left|\frac{s_{21}(\theta,\phi)}{s_{21}(\theta_1,\phi_1)}\right|^2, \tag{2}$$

[2]In some literature, the port mismatch is not included in the radiation efficiency and the net power accepted by the antenna is considered.

[3]The field pattern of the antenna quantifies the magnitude of the field instead of power and thus is the square root of the power pattern.

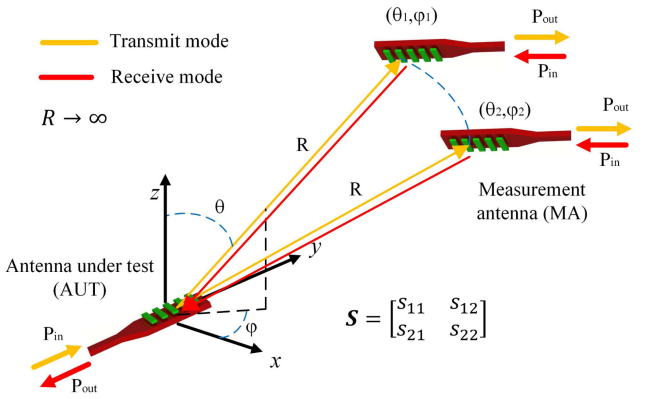

Fig. 2. Antenna setting for deriving radiation pattern in the transmit mode and effective aperture pattern in the receive mode. Radiation pattern, $D(\theta, \phi)$, and receiving pattern, $A(\theta, \phi)$, of an antenna in a reciprocal medium are linearly related.

in which (θ_1, ϕ_1) is the reference angle (usually the angle with maximum power). Conversely, with AUT in the receive mode, the MA radiates power and the AUT receives it. Now, the power transfer from MA to AUT is given by $|s_{12}(\theta, \phi)|^2$. The effective aperture pattern (receive pattern) $A_{\text{eff}}(\theta, \phi)$ is proportional to

$$A_{\text{eff}}(\theta, \phi) \propto \left| \frac{s_{12}(\theta, \phi)}{s_{12}(\theta_1, \phi_1)} \right|^2. \tag{3}$$

In a reciprocal medium, the scattering matrix is symmetric, i.e. $s_{12} = s_{21}$ [22]. Therefore, the directivity pattern in the transmit mode and effective aperture pattern in the receive mode are linearly related as

$$A_{\text{eff}}(\theta, \phi) \propto D(\theta, \phi), \tag{4}$$

Hence, the well-known relation between directivity and effective aperture for a single-port antenna that can be obtained by calculating the effective aperture and directivity pattern of an arbitrary antenna which yields [23]

$$A_{\text{eff}}(\theta, \phi) = \frac{\lambda^2}{4\pi} D(\theta, \phi), \tag{5}$$

in which λ is the wavelength of the electromagnetic wave. In other words, the normalized radiation pattern of the antenna in the transmit mode and its effective aperture pattern in the receive mode are the same. Therefore, a single-port antenna that has a good performance in sending the wave towards a certain direction is also a good antenna for collecting the light impinging from the same direction.

The limit on the maximum aperture of a single element within a large array dictated by the element spacing due to conservation of energy that was mentioned earlier can be equivalently expressed as a limit on the maximum directivity. Together with (5), this leads to the following maximum directivity limit for a single element within a large regular array:

$$D_e \leq 4\pi \frac{d^2}{\lambda^2}, \tag{6}$$

where d is the element spacing.

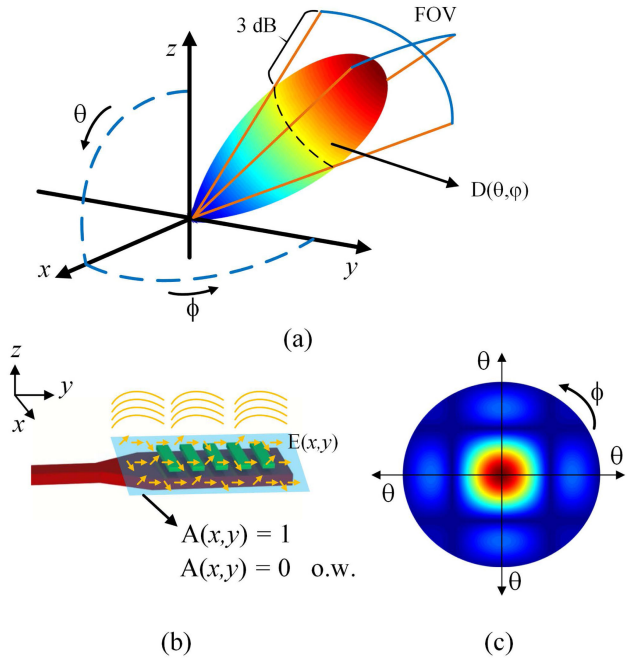

Fig. 3. (a) Radiation pattern of a transmitter antenna with -3dB range FOV (b) Conceptual schematic of the aperture electric field distribution, $E(x, y)$, windowed by the aperture function, $A(x, y)$ (c) *sinc* function far-field pattern of the aperture windowing effect which is equivalent to windowing a plane wave traveling in the z direction.

III. Fabrication Imposed Limitations

Aside from the fundamental trade-offs in designing a nano-photonic antenna (discussed in the next section), the single photonic layer platforms, offered by many low-cost silicon photonic foundries, impose further limitations on adjusting and improving the effective aperture and FOV of the antenna. Therefore, in this section, we study the performance parameters of nano-photonic antennas and discuss the limitations of a general form antenna in a silicon photonic platform. Moreover, potential antenna structures to push the performance to conventional fundamental limits are demonstrated. Since the radiation pattern and effective aperture pattern are linearly related, equation (5), maximizing antenna's radiation efficiency and directivity yields the maximum effective receiving aperture as well. However, since investigating antenna characteristics in the transmitter setting is more illustrative, the following discussion is examined from the transmitter point of view.

Since dielectric antennas can be safely approximated as lossless, low reflection at the input port of the antenna results in high antenna efficiency. Therefore, the input port of the antenna structure should provide an acceptable matching[4] to maximize the radiated power by the antenna in the transmit mode and correspondingly, its effective aperture in the receive mode. In addition to coupling the input power to the antenna efficiently, its radiation pattern should be adjusted. The antenna pattern or far-field radiation pattern, Fig. 3(a), is the same as its aperture Fraunhofer diffraction pattern. In other words, the antenna field

[4] S_{11} of less than -20 dB is considered acceptable in many situations [22].

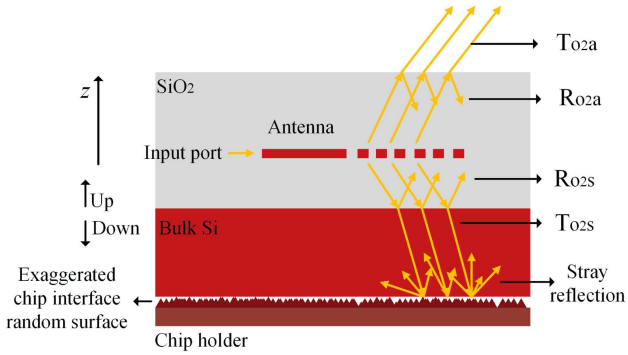

Fig. 4. A conceptual side-view schematic of the transmitter antenna on a silicon photonic platform with bottom reflections from the Box-Bulk interface and the bottom of the chip.

pattern is the Fourier transform of the field distribution on the antenna aperture [24]. FOV of an antenna is an angular range on the antenna pattern with a power density higher than a specific threshold (usually considered -3dB lower than the maximum). Since antenna radiation pattern and effective aperture pattern are linearly related, the FOV of the antenna in the transmitter and receiver settings are the same. To derive the relationship between the antenna geometry and FOV, the electric field distribution of the aperture can be thought of an electric field distribution $E(x, y)$ multiplied by an aperture function $A(x, y)$. Therefore, the far-field field pattern is the convolution of the Fourier transforms of $E(x, y)$ and $A(x, y)$. Since for a smaller aperture size $A(x, y)$ has a wider Fourier transform, it is expected that a smaller antenna size yields larger FOV and a larger antenna size with a larger aperture results in a more directive far-field pattern and narrower FOV.

While this is a simplified but effective relationship between the antenna size and its FOV, the size of the antenna does not yield any information about the specific angular range that the radiated power is directed to. The shape of the antenna pattern depends on the E-field distribution on the antenna aperture. If the aperture window function is approximated with a rectangular function, a uniform electric field distribution on the aperture (which is the case for a windowed plane wave traveling in the positive z-direction in Fig. 3(b)) yields a far-field pattern which is a *sinc* function centered at $\theta = 0$ (Fig. 3(c)). However, the direction of the guided mode is orthogonal to the z-direction in integrated photonics. Therefore, a grating coupler as a conventional nano-photonic antenna embeds a periodic structure inside the antenna aperture that modulates the spatial frequency of the electric field and adjusts the far-field pattern direction of the antenna by shifting the Fourier spectral content (far-field pattern) by the spatial modulation frequency. However, since the antenna is fed from one side, the field distribution might deviate from an ideal periodic pattern. While using a grating structure is a straight forward technique to achieve a field distribution, other designs obtained by aperiodic and irregular apertures have been also demonstrated recently [4], [18], [25].

In a simple slab antenna, there is radiation from the top and bottom of the aperture (positive and negative z), as in Fig. 4. With the silicon substrate underneath the antenna, the reflected wave from the bulk-BOX interface changes both the aperture function, $A(x, y)$, and distribution of the electric field, $E(x, y)$. The reflection potentially has a wider field distribution and can interact with the neighboring structures and increase the mutual coupling between the antennas in an array. Moreover, the reflected light may travel in a different direction after interacting with the antenna structure again, affecting the antenna pattern. If part of the power radiates in undesired directions, it can cause unwanted peaks in the radiation pattern with undesirable effects. The light that passes through the bulk at the interface hits the bottom of the chip and reflects, as illustrated in Fig. 4 in a simple ray-optics view. This reflection becomes more unpredictable if the interface is not very smooth and can lead to a random pattern, making it very difficult for the elements to produce a repeatable pattern that will limit the system functionality. Since transmit-mode radiation pattern and receive-mode effective aperture are linearly related, these effects disrupt the receiving functionality of the antenna as well. Therefore, it is desirable to design the antenna so that it couples the light maximally upward to achieve the best directivity and effective aperture, which presents its own challenges in a single-layer low-cost photonic process.

Consider a single layer photonics process that allows for 2D waveguide routing in addition to a few etching masks operating at a wavelength of 1550 nm with waveguide dimension of 220 nm height and 500 nm width. Without an additional etching mask, the only asymmetry in the antenna structure would be due to the silicon substrate at the bottom versus the air interface on the top. To obtain an estimate of the upper bound on the antenna performance in this setting, the reflection and transmittance from silicon oxide into silicon and air for normal angle can be simply calculated based on the Fresnel equations as

$$R_{o2a} = \left|\frac{n_{ox} - n_{air}}{n_{ox} + n_{air}}\right|^2 = 0.03,\ T_{o2a} = 0.97, \tag{7}$$

$$R_{o2s} = \left|\frac{n_{si} - n_{ox}}{n_{si} + n_{ox}}\right|^2 = 0.16,\ T_{o2s} = 0.84, \tag{8}$$

in which $n_{ox} = 1.44$, $n_{si} = 3.4$, and $n_{air} = 1$ are the the refractive indices of silicon oxide, silicon, and air, respectively. If we assume that the reflected wave from the bulk silicon (with reflection coefficient R_{o2s}) does not interfere considerably with the upward radiation of the antenna (T_{o2a}) and ignore the secondary reflections inside the oxide slab, then for the best case, the total light power radiated upward is

$$T_{up} = (0.5 \times 0.97 + 0.16 \times 0.5 \times 0.97) = 56\%. \tag{9}$$

Constructive interference of the reflected wave and the upward radiating wave can improve the amount of power that will be radiated to the air. However, due to the widening of the reflected beam, the two beams do not overlap or interfere constructively for the most part. Therefore, the above derivation is a close approximation to the practical power efficiencies that are achievable. Even with additional etching levels, only a limited amount of vertical asymmetry can be achieved. For instance, an additional 110 nm etch into a 220 nm silicon slab is still less than $\lambda/4$ with λ being the wavelength of the light inside silicon,

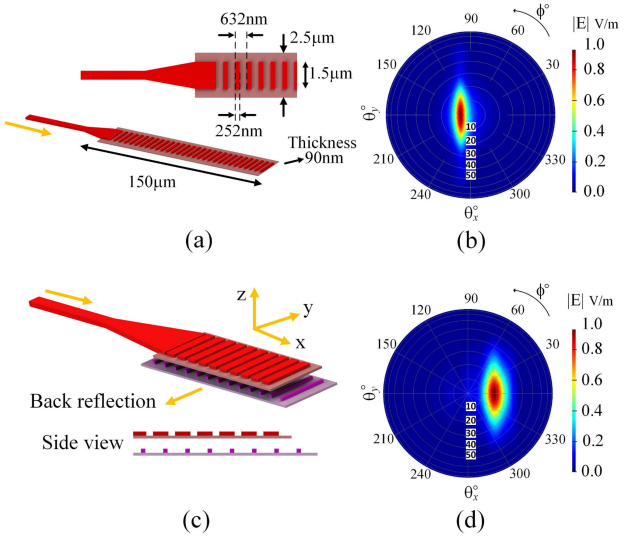

Fig. 5. (a) & (b) 1D-FOV antenna with 60% upward radiation efficiency with its radiation pattern (c) & (d) Schematic of the 2D-FOV antenna with boosted asymmetry for improved performance and its radiation pattern achieving 80% upward radiation efficiency.

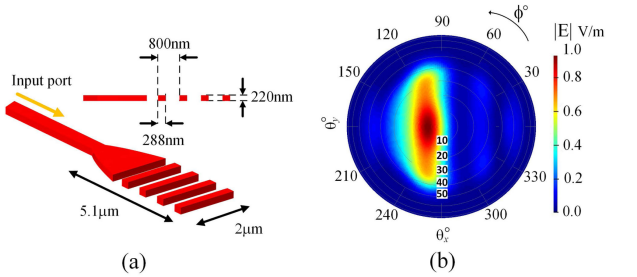

Fig. 6. A regular symmetric 2D-FOV grating based antenna with 4 grating slabs achieving 35% efficiency after optimization.

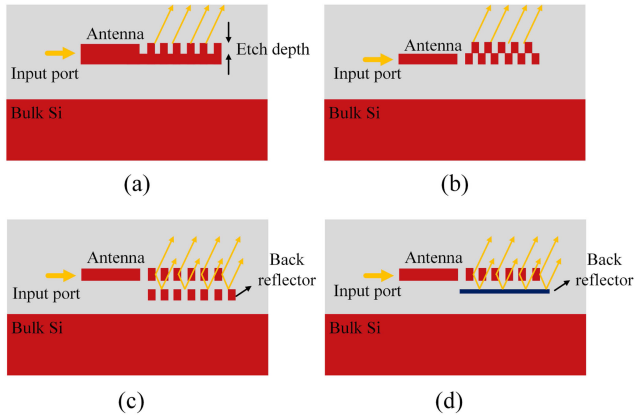

Fig. 7. Various forms of increasing the asymmetry to improve radiation efficiency (a) using a thicker silicon layer (b) adding a silicon layer on the antenna (c) & (d) adding a bottom reflector.

455 nm. Therefore, the electromagnetic wave does not face an effective distinction between the two sides. Fig. 5(a) & (b) show the best performance achieved by optimizing an antenna with a narrow FOV in one dimension in such a single-layer photonic process, which leads to 60% upward radiated power. To improve the radiation efficiency in this setting (with the maximum silicon slab thickness of 220 nm), structures with accentuated asymmetry such as *two-layer grating couplers* [26], [27] should be devised.

The above derivation for a long antenna structure results in a one-dimensional FOV antenna assuming all the power being radiated upward or downward. The long and skinny shape of the antenna and thus its aperture function $A(x, y)$ results in narrow FOV in the long direction of the antenna through the 2D Fourier transform of the aperture shape. We will refer to such antennas whose FOV extends in one dimension but is narrow in the other as "1D-FOV" antennas. This will be in contrast to antennas with wide FOV in both directions, to which we will refer as "2D-FOV" antennas.

It is clear from the basic properties of the Fourier transform that to achieve a wide 2D-FOV antenna, it should be small in both dimensions. For $\lambda = 1550\,\mathrm{nm}$ this results in relatively small antennas (less than 6 μm). The price for such a short antenna structure is that a fraction of the forward propagating guided wave continues without being coupled out, possibly causing other challenges such as stray light after interacting with other structures on the chip. For example, the simple grating-based antenna in [7] with 3 to 4 grating slabs, which represents a practical 2D-FOV radiator, splits the power between upward, downward, and forward radiation components almost equally, leading to a radiation efficiency of roughly 30% to 37% with the added disadvantage of having two-thirds of the power resurfacing as stray light. Fig. 6 shows such an antenna optimized for the maximum radiation efficiency achieving 35% upward radiation. Modification of the antenna aperture structure and deviating from the grating-based design can yield higher radiation efficiency such as the antenna demonstrated in [4] achieving 51% radiation efficiency.

A stronger asymmetry in the structure of the antenna is needed to improve the radiation efficiency. For example, a thicker than $\lambda/2$ silicon slab with etching layers can achieve a higher asymmetry and thus more efficient upward radiation as shown in Fig. 7(a) & (b). Another approach to introduce asymmetry is adding extra dielectric layers in the fabrication process, Fig. 7(c) & (d). To demonstrate the potential improvement that can be achieved using a stronger asymmetry, we designed a compact 2D-FOV antenna shown in Fig. 5(c) & (d). This design shows an example of vertical directivity enhancement to 80% utilizing a silicon back-reflector layer.

There have been attempts in the past to design transmitter antennas with higher radiation efficiency which are limited to 1D-FOV structures. In [8], a high-contrast grating structure is used to improve the performance and a radiation efficiency of 94% is reported at 1550 nm wavelength. Moreover, antenna designs with an extra dielectric layer to obtain a controlled and improved reflection were demonstrated that achieve close to 90% radiation efficiency [5], [6], [10]. While the specific details of the approaches taken in these works are different, in principle the core idea is to introduce an asymmetry in the structure of the antenna to improve its radiation efficiency. Therefore,

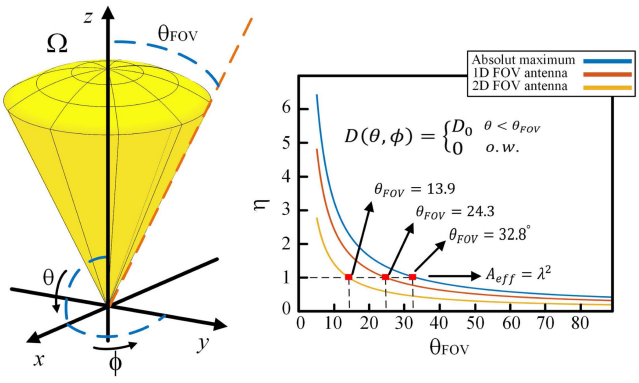

Fig. 8. (a) Idealized directivity pattern with FOV of $\theta = 2 \times \theta_{FOV}$ (b) η factor versus θ_{FOV} that shows for an effective aperture of λ^2, the maximum achievable FOV is $\theta_{FOV} = 32.8^{\circ}$. FOV achievable for 1D antennas in low-cost silicon photonics processes is $\theta_{FOV} = 24.3^{\circ}$ and FOV achievable for 2D antennas in low-cost silicon photonics processes is $\theta_{FOV} = 13.9^{\circ}$.

other techniques that can overcome some of these limitations by design, without the need for additional dielectric layers, would be highly desirable as the added layers increase the fabrication cost and complexity.

IV. Trade-Off Between Effective Aperture and FOV

As discussed earlier, designing a receiver antenna with a large effective aperture is desired in many applications to achieve a larger signal-to-noise ratio. Moreover, it is often desirable for the antenna to be able to collect light from a large FOV, particularly if beam-steering is desirable. However, designing an antenna with both large effective aperture and FOV faces some fundamental limits in a reciprocal system which is the case for standard materials used in silicon photonic processes. Next, we briefly review this limit using an idealized model and then discuss its implications leading to additional design insights.

For the idealized model, we assume that the radiated power is distributed uniformly on a solid angle of Ω bounded by $\theta < \theta_{FOV}$, as shown in Fig. 8(a). Since power is only radiated within Ω (instead of the full sphere of 4π solid angle), directivity increases by a factor of $4\pi/\Omega$ within Ω compared to an isotropic radiator (uniform directivity of 1) and is zero outside. Therefore, the directivity pattern is calculated as

$$\Omega = \int_0^{2\pi} d\phi \int_0^{\theta_{FOV}} \sin(\theta) d\theta = 4\pi \sin^2\left(\frac{\theta_{FOV}}{2}\right), \quad (10)$$

$$D(\theta,\phi) = \frac{4\pi}{\Omega} = \csc^2\left(\frac{\theta_{FOV}}{2}\right), \quad (11)$$

which in combination with (5) leads to an effective aperture of

$$A_{\text{eff}} = \left(\frac{\lambda}{\sqrt{\Omega}}\right)^2 = \left(\frac{\csc\left(\frac{\theta_{FOV}}{2}\right)}{2\sqrt{\pi}}\lambda\right)^2 = (\eta\lambda)^2, \quad (12)$$

where η^2 is the effective aperture normalized by wavelength squared. (e.g., $\eta = 1$ corresponds to an effective aperture of λ^2.) Fig. 8(b) shows η versus the FOV of the antenna. For $\eta = 1$, θ_{FOV} is 32.8° corresponding to a FOV of 65.6°. If the radiation pattern has the ideal conical shape similar to Fig. 8 but not centered at $\theta = 0$, the derivation yields the same result for the same solid angle value of Ω. A larger η (larger effective aperture) comes at the cost of smaller FOV. This is the fundamental trade-off between the effective aperture and FOV of a single-port single-mode receiving antenna. This idealized antenna pattern is a useful, yet practically unrealizable abstraction. The inverse Fourier transform of the pattern that corresponds to the electric field distribution on the surface of the antenna aperture has infinite area due to the brick-wall drop of the radiation pattern, making it unrealizable exactly due to the finite dimensions of any physical antenna. Any finite-size antenna will have side lobes outside the primary radiation beam and will not have a perfectly uniform radiation pattern within the FOV, often defined by the full-width-half-maximum beam width (3dB drop). The added power outside the FOV further reduces the average directivity within the FOV. This leads to an average effective aperture in the FOV smaller than the ideal model of Fig. 8(a), while the non-uniformity of the effective aperture can lead to a larger effective aperture at the peak of the pattern. Any side lobe or stray radiation outside of the FOV reduces the directivity and thus the effective aperture inside the FOV, highlighting the need for a well-designed radiation pattern.

In light of the relationship of equation (5), the discussion about the physical size of the transmitter antenna and its FOV in section III can be extended to the receive mode. For the transmitter antennas, increasing the physical size of the antenna leads to a smaller FOV due to the Fourier transform's scaling property. The equivalent of this statement in the receive mode is that a larger physical size can increase the effective aperture and the collected power at the cost of a smaller FOV. Therefore, in designing a single-port single-mode receiver antenna, if the effective aperture is increased by increasing the physical size of the antenna, the angular range that the antenna can collect power from decreases accordingly.

V. Designing Antennas Beyond Conventional Performance Limits

An antenna performance beyond conventional limits could only be achieved by overcoming the trade-off between FOV and effective aperture that was derived in (5). This would only be possible by violating the assumptions leading to (5). The single-mode antenna port assumption for the configuration of Fig. 2 resulted in the two-port network model, which forms the foundation of our derivation. Extending the antenna structure to support multi-mode guided waves may open a path for designing antennas with performance metrics beyond the conventional limits. To capture the effect of the extra modes of the antennas in the scattering matrix model, a new row and column should be added for every extra mode on each antenna. Following the same procedure in section II, it can be shown that for a reciprocal medium, the relationship of equation (5) still holds for every pair of transmitter-receiver modes, individually. However, the contribution of different modes *collectively* can yield a larger effective aperture and FOV, simultaneously. In other words, adding a second mode to the antenna could in theory up to double the FOV (in solid angle) with the same effective aperture. Alternatively, it

could up to double the effective aperture with the same FOV or increase both FOV and effective aperture partially. Increasing the number of modes supported by the antenna relaxes the trade-off with the same trend by each mode bringing its share of FOV and effective aperture. It is worth noting that dual-polarization grating couplers investigated in the literature [28]–[30] are a small subset of multi-mode antenna structures. In these couplers, the two orthogonal incident polarizations are captured by the two antenna modes and coupled into the super-modes formed by two single-mode waveguides.[5] While the peak value of the effective aperture is not increased, it is extended to cover the whole polarization state-space uniformly rather than having a peak at a single polarization and dropping to zero for the corresponding orthogonal polarization. As a side note, another assumption leading to (5) is the reciprocity of the medium, which can potentially be broken by incorporating non-reciprocal materials in the antenna structure. While an interesting topic for further research, we will focus on the multi-mode antennas in the rest of this manuscript due to the current integration challenges and loss properties of non-reciprocal materials.

The multi-mode antennas are studied in the microwave region and used for various purposes such as designing loaded scatterers [31], [32], pattern synthesis [33], realizing antennas for multiple-input multiple-output (MIMO) systems [34], [35], etc. For metallic antennas operating in the microwave region, design methods such as characteristic modes can be used to analyze the antenna and realize single- and multi-mode antennas [36]–[38]. A class of electromagnetic structures that share similarities with multi-mode antennas are multi-beam antennas. In microwave antenna design, multi-beam antenna is referred to a *collection* of independent antennas that can send independent waves in different directions [39].

It should be noted that in a reciprocal medium, the power collected and coupled to multiple modes can not be fully combined into a single mode and carried by a single-mode waveguide, as that entire system would be tantamount to a single-mode single-port antenna. While an ideal electromagnetic power combiner does not exist [22], it is possible to combine the power of multiple modes into a single one, if the phases and amplitudes of the input modes are defined or controlled [40] and novel techniques such as inverse design and computational design method can be used to improve the performance [41]–[43]. However, in the case of the multi-mode antenna, the relative phase and amplitude of the excited modes changes versus the incident angle and rules out this possibility. In other words, such a power combiner cannot be lossless or it will not have matched ports that causes power reflection at the ports, Fig. 9(b) & (c). This fact can be easily understood by changing the boundaries of the network and including the combiner inside the system, which yields an antenna with a single-mode port and leads to the limitations discussed. Therefore, the collected power should either be transferred using a multi-mode waveguide or should be down-converted by photodetectors first and then combined,

[5]It is called a super-mode because the field profile of the mode can be considered as (or due to the weak coupling closely approximated by) the superposition of the single isolated modes.

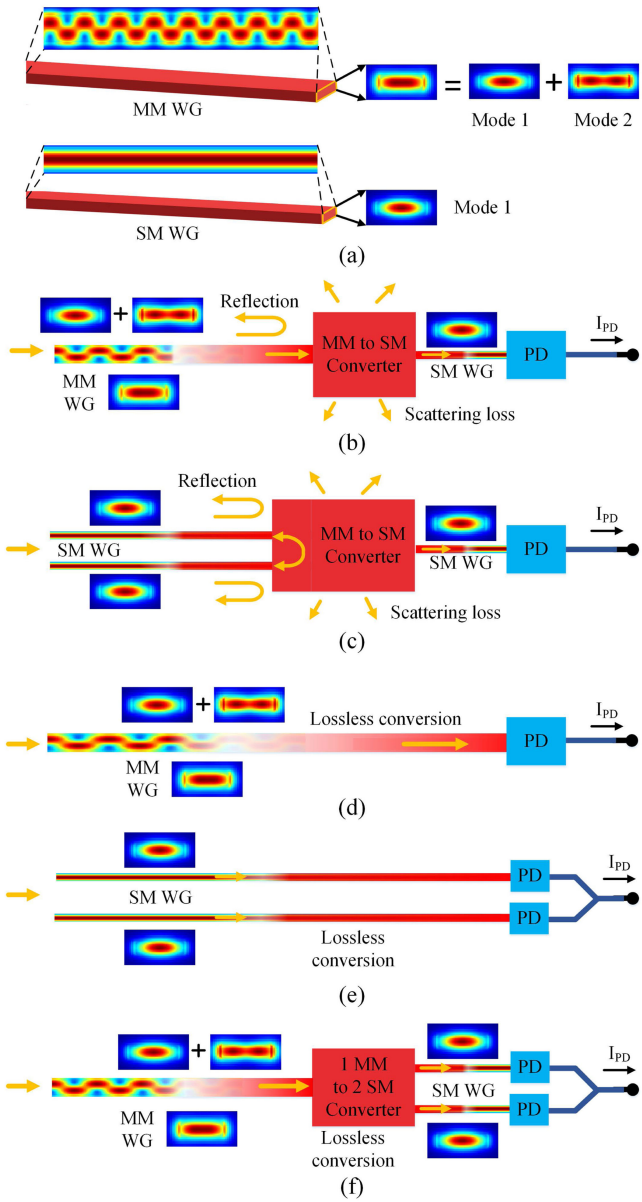

Fig. 9. (a) Multi-mode and single-mode waveguides (b) The two modes carried by a multi-mode waveguide combined into a single mode waveguide. (c) The two super-modes supported by the two single-mode waveguide combined into a single mode waveguide. (d) The power carried by a multi-mode waveguide input to a power detector that outputs the combined power. (e) The two super-modes of the structure are input to two power detectors and power combining happens after down-conversion to DC. (f) A multi-mode to multi-mode (super-mode of two single modes) is used before feeding the power into the photodetector.

Fig. 9(d) & (e). The non-linearity of the photo-detection process breaks the assumptions in our derivations and invalidates the discussed constraints. While lossless conversion of multiple modes into a single-mode is not possible, converting n modes carried by a structure into n or more modes supported by a different structure is possible. Examples of such mode converter structures are presented in [44]–[47] which convert the two modes of a multi-mode waveguide into two super-modes supported by two single-mode waveguides. Therefore, to improve the photodetection process, multi-mode to multi-mode conversion can be used first, Fig. 9(f).

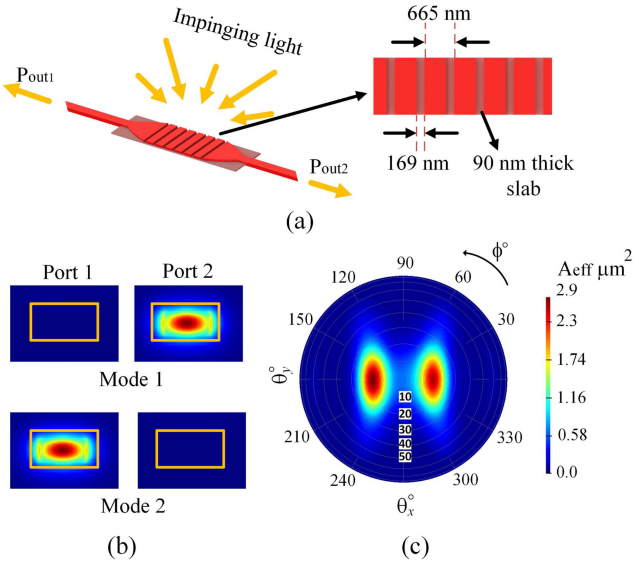

Fig. 10. (a) Dual-mode antenna which uses two single mode waveguides to form two super-modes carrying the optical power output by the antenna (b) Cross section of the supper-modes of the antenna propagating in the waveguides (c) Total FOV and effective aperture of the antenna versus azimuth and elevation angles.

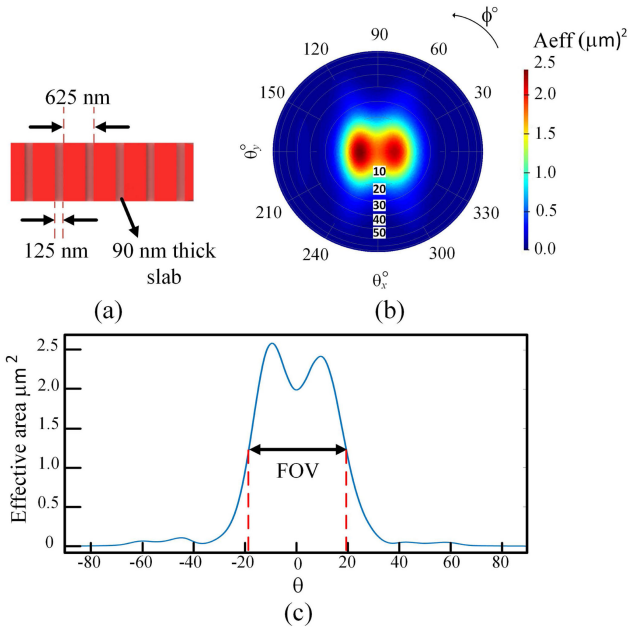

Fig. 11. (a) Design parameters of the dual-mode antenna with a monotonic FOV (b) Total FOV and effective aperture of the antenna versus azimuth, ϕ, and elevation, θ, angles (c) Effective area of the antenna versus θ for $\phi = 0$ which shows a 40° of FOV.

There are various possible design options to extend the antenna structure for supporting more than one mode. A simple illustrative structure is the dual-port antenna of Fig. 10(a), where a super-mode is formed using two single-mode waveguides such that the field distribution of each waveguide is not disturbed. This is done by placing the two waveguides on opposite sides of the antenna. The two states of the super-mode formed by the two waveguides are shown in Fig. 10(b) which can be approximated with the individual modes of the two waveguides with high accuracy. To keep the design simple and the number of degrees of freedom small, a periodic grating of 6 silicon slabs is used to shape the field distribution on the antenna aperture. Since only two modes are assumed, the design space provided by the grating structure is flexible enough to yield high radiation efficiency and effective aperture for both modes. To maximize the FOV, the FOV range of the two modes are designed to be separated, Fig. 10(c). Therefore, the FOV of the antenna is doubled compared to a single-mode antenna of the same kind in a low-cost silicon photonics process. The grating period is 665 nm with 25% duty cycle. Moreover, an etched silicon slab facilitates the forward propagation of the field as well as providing a good matching at the input ports. This antenna achieves a peak effective area of 2.9 μm^2 with total FOV of 30° by 30°.

Separation of the FOV of the two modes maximizes the functional angular range of the antenna but results in a deep notch at 0°. Using the same structure, it is also possible to achieve a monotonic angular range for FOV and adjust the ripple of effective aperture/directivity inside the FOV range. Fig. 11 shows a design with a single large angular range of FOV of 40° by 15° achieving effective area of 2.5 μm^2. Since the FOV of the two modes overlap, the peak effective aperture regarding the total collected power by the two modes can be more than the design of Fig. 10. In other words, since the trade-off is relaxed by a factor of two in the 2-mode structures, if FOV is reduced the effective area inside the FOV will increase.

Extrapolating the methodology used for the dual-port antenna of Fig. 10 and Fig. 11, an example of a 3-mode antenna is shown in Fig. 12(a). It constructs super-modes using three single-mode waveguides with 0.5 μm gaps between them to increase the product of FOV and effective aperture. The three waveguides collectively support the three modes of the antenna port, as shown in Fig. 12. For adjusting the electric field distribution on the antenna aperture, a standard grating structure has a limited design space in this case and cannot be used to achieve good performance over a broad range of angles. Therefore, we adopted a patterned dielectric slab for the antenna area and exploited an optimization method to generate an etching pattern on the slab. The etching pattern consists of 150 nm blocks that are either etched or left unetched. Therefore, the etching pattern can be represented by a binary pattern, which makes genetic algorithm a suitable optimization method for the problem [4]. The physical antenna aperture is chosen as a relatively small square size of 3.8 μm by 4 μm. Therefore, FOV of each mode is larger than the 2-mode antenna presented above. The effective aperture of the antenna is shown in Fig. 12(c) exhibiting a broad FOV range with a peak effective aperture of 1.6μm^2. Fig. 12(c) also shows the effective aperture versus angle for the three modes individually which illustrates the contribution of each mode in the overall power collection capability of the antenna.

Constructing a super-mode using multiple uncoupled single modes yields a larger antenna footprint as the number of modes increases. An alternative structure is an antenna with a single physical port that supports multiple modes. To collect the output signal of the antenna, a single waveguide that supports those modes and is matched to the input port of the antenna at each

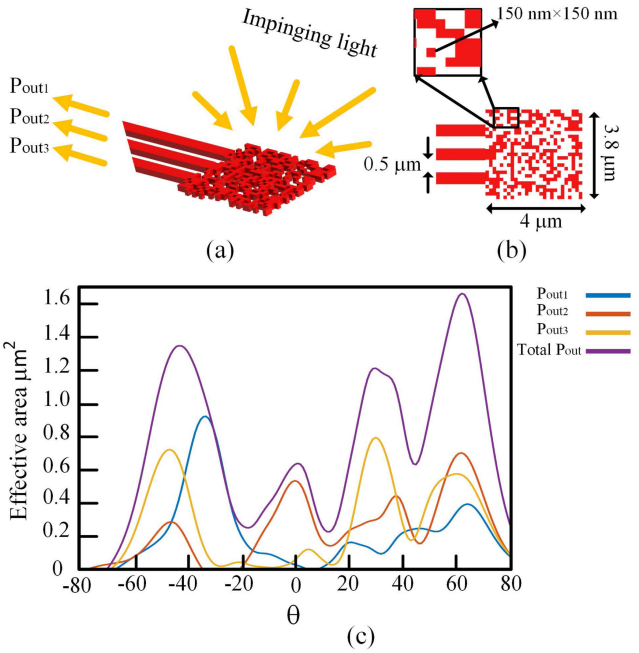

Fig. 12. (a) Schematic of the designed 3-mode antenna which uses three single mode waveguides to form the super-modes carrying the optical power output by the antenna. (b) Design details of the antenna aperture formed by etching a binary pattern of 150 nm squares. (c) Total effective aperture and individual effective aperture provided by each supported mode versus elevation angle.

mode is needed. In a standard silicon photonics process with a silicon layer thickness of 220 nm, the width of a single-mode waveguide is 0.5 μm and larger waveguide width introduces more modes that are supported by the waveguide. Since the group indexes of different modes of a multi-mode waveguide differ a lot, a grating structure is not very effective to construct the antenna aperture and a patterned slab similar to Fig. 12 is needed to achieve high performance.

While an integrated planar multi-mode antenna significantly increases the collection area compared to the conventional nano-photonic antennas, non-planar antenna designs can potentially lead to solutions with higher fill factor and broader FOV due to the addition of the third dimension that can be used to support additional modes. To demonstrate this possibility through an example, we propose a multi-mode silicon pillar antenna with a square cross section of 630 nm by 630 nm surrounded by silicon oxide. Although air as the surrounding material results in better confinement of the optical field in the silicon pillar, silicon oxide is used here for better mechanical stability and fabrication yield. The dimensions and the higher dielectric constant of silicon compared to the surrounding silicon oxide defines the supported modes of the antenna. The antenna supports four pairs of modes and each pair covers two orthogonal polarizations of the same kind, as in Fig. 14(a)–(h). The difference between the electric field distribution of the mode profiles, the amplitude distributions as well as their phase distributions, leads to a different far-field radiation pattern for each mode, where the effective aperture of each mode covers different angular ranges. The reciprocity theorem can be used for each mode separately to obtain the antenna effective aperture corresponding to that

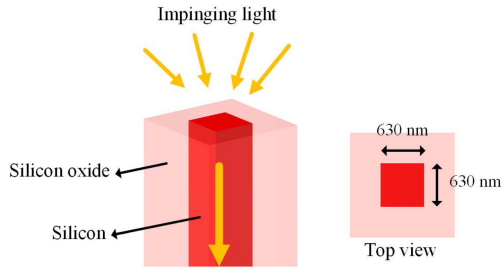

Fig. 13. A single pillar as a non-planar antenna that supports 4 mode pairs that each pair collect power from two orthogonal polarization.

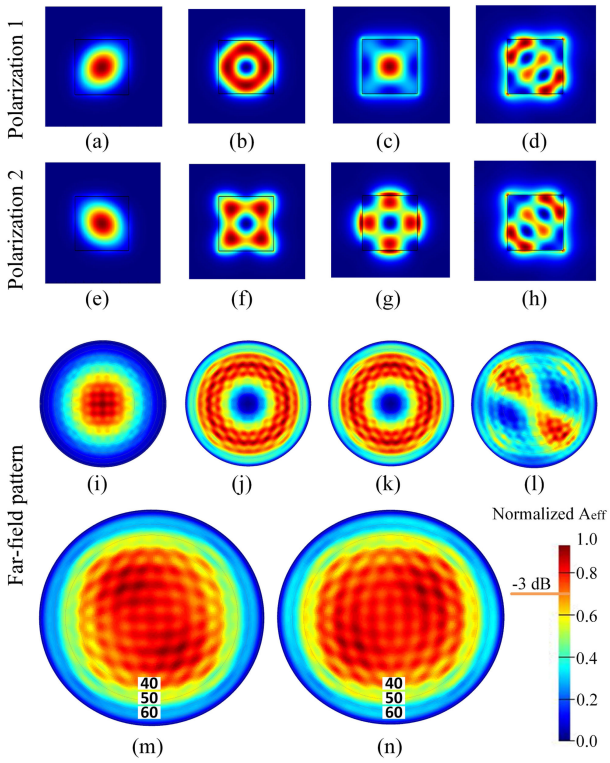

Fig. 14. The graphs are normalized and the color bar shows the relative intensity. (a)–(d) Modes of the polarization set 1 (e)–(h) modes of the polarization set 2. (i)–(l) Effective area of the polarization set 1 modes (effective area for the set 2 is counterpart of these graphs). (m) Collective effective area of set 1. (n) collective area of set 2.

mode, which are shown in Fig. 14(i)–(l). The collective effective aperture for the two polarization sets are shown in Fig. 14(m) and (n) achieving a broader overall antenna FOV.[6] As mentioned in section II, a single-mode antenna has a maximum collection area for a particular polarization and zero collection capability for the orthogonal one for any given (θ, ϕ). However, in this structure, not only a large FOV is achieved, but also the pillar antennas have large effective aperture and FOV for both polarizations of the incident wave.

The compact form factor of this pillar antenna makes it a suitable candidate for a dense receiver array aperture with

[6]The radiation patterns associated with different modes have finite overlap, which can never be fully eliminated [48]. However, such overlap does not present a fundamental challenge to increasing the FOV.

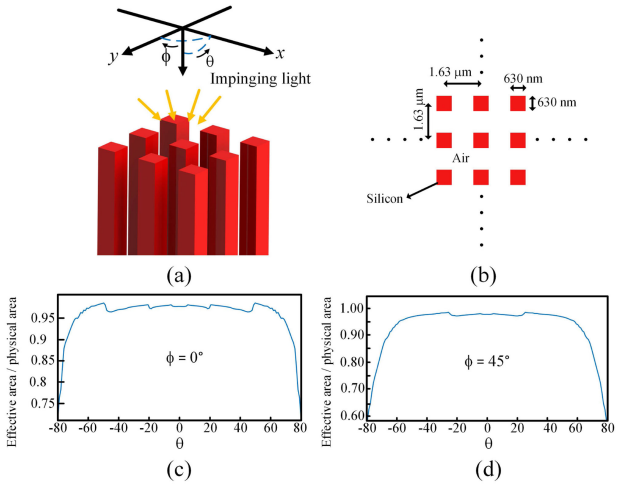

Fig. 15. (a) Dense array of pillar antennas (b) top view of the array with dimensions of each unit cell (c) & (d) power collection efficiency of the nit cell versus azimuth angles 0° and 45°.

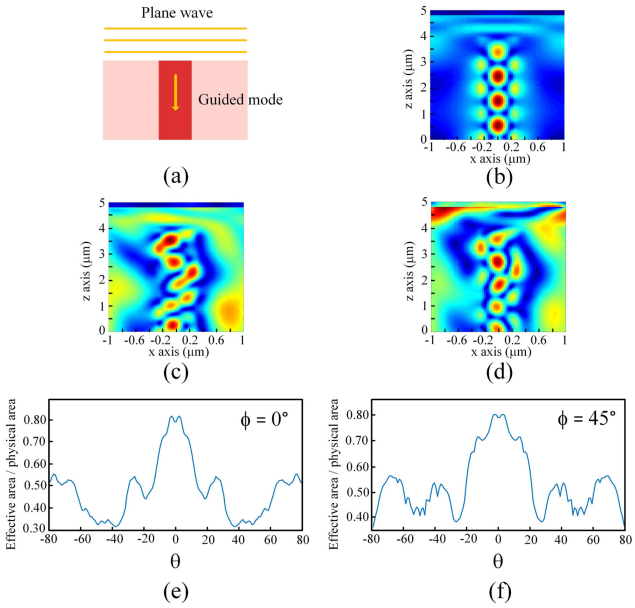

Fig. 16. Power collection efficiency of the array in a 0.6 μm by 0.6 μm window around the pillar antenna (a) azimuth angle = 0° (b) azimuth angle = 45°.

broad FOV and large fill factor. Due to the large index contrast of silicon with the surrounding oxide medium, the modes of the single antennas will not get affected significantly by the neighboring array elements [49], and the major modes of the array will essentially resemble the modes of a single antenna. Fig. 15(a) shows the antenna array incorporating pillar antennas as array elements. The element spacing of the array and the dimensions of the antenna are optimized to maximize the power collected by each unit cell. The ratio of the collected power by each unit cell to the total incident power (Fig. 15(b) & (c)) is more than 95% for a broad range of FOV exceeding 140° by 140°. It should be noted that the effective area of each antenna is close to its upper bound in an array, as discussed previously. Noticeably, both FOV and effective apertures are pushed to their limits independently in this architecture.

In a photonic receiver array, the area of the photo-detector is generally a fraction of the unit cell due to the space occupied by various other photonic and electronic components as well as metal interconnects and interfaces. To achieve a large fill factor, an antenna should receive and confine the incident light into a smaller volume so that it can be coupled into the photodetector efficiently. Hence, the dimensions of the pillar antenna and the array element spacing are optimized such that it confines the optical power into a 0.6 μm by 0.6 μm window in the vicinity of the pillar while maintaining a large effective aperture. While the exact sizing of the focusing window is determined by the photodetector area in the unit cell, the 0.6 μm by 0.6 μm window size is a good estimate for the detector size (considering the wavelength-scale unit cell size to have a dense enough array for sampling the wavefront) to demonstrate the focusing capability of the antennas. Fig. 16 shows the power focusing capability of the array into a small region of the antenna. Since the propagation speeds of different modes are not the same, a periodic intensity distribution is formed that peaks where all the modes are in phase. Since the effective apertures of the modes vary versus the reception angle, the relative magnitude of the modes changes accordingly. Therefore, the focusing capability of the antenna is affected for larger angles. A metric for an effective aperture of the focusing, which takes into account only the fraction of the power in the 0.6 μm by 0.6 μm window is a more precise measure of the performance of the antennas in an array. Fig. 16(e) & (f) show the focusing effective aperture of the antenna versus the reception angle. While the uniformity of the effective aperture is not the same as the full unit cell, the 3dB FOV of the aperture exceeds 160°. The full width at half maximum (FWHM) window size of the focused power is 0.58 μm by 0.58 μm which contains 72% of the total power received by the unit cell. This corresponds to the effective area of 1.92 μm^2. The performance of such a radiator must be evaluated within the array, as the interactions with the adjacent element change the individual antenna behavior compared to a standalone pillar. Therefore, each unit cell is an antenna unit with periodic boundary conditions. For a photodetector size of $0.58 \times 0.58\ \mu\text{m}^2 = 0.34\ \mu\text{m}^2$, the dielectric antenna array increases the effective multi-mode collection area by

$$\eta_{ap} = \frac{A_{\text{eff}}}{A_{phy}} = 5.7, \tag{13}$$

in which A_{eff} is the effective collection area and A_{Phy} is the physical area of the photodetector. Large aperture efficiency and FOV suggest the application of this structure for a dense optical phased array coherent receiver. To further clarify the merits of this structure, it can be compared to the recently published optical phased array receivers [7] which uses conventional nano-photonic antennas in an array for collecting the incident power. The antenna in [7] has 0.92 μm^2 of peak effective aperture at -6° with unit cell size of 11.2 by 11.2 μm^2, where it achieves an aperture efficiency of 0.0074 while the array element spacing limits its FOV to 8°.

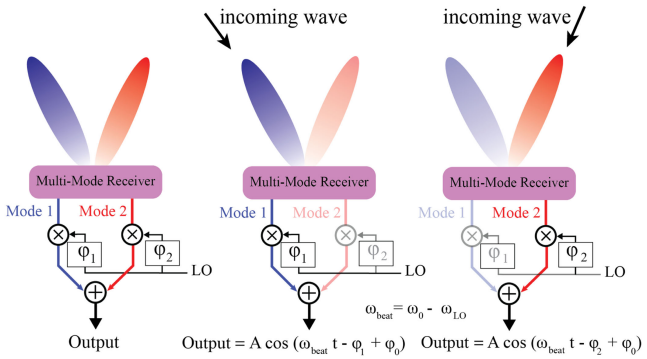

Fig. 17. Heterodyne detection system model in multi-mode antennas.

VI. Coherent Detection With Large FOV and Large A_{eff}

The proposed multi-mode pillar antennas forming a wide-FOV dense receiving array are not only compatible with a direct detection architecture (implicitly discussed above), but also can be used with a heterodyne detection scheme to realize a coherent imager by recording both phase and amplitude information of the wavefront. Nano-photonic receiver architectures featuring heterodyne detection have been shown to achieve high sensitivity, and robustness to interference and noise which makes them a suitable candidate for various applications such as imaging [7] and ranging. Fig. 17 shows the system level diagram of the proposed multi-mode coherent detection array in which each port represents a single mode and each mode has its own received pattern. If an optoelectronic mixer [7] is used before the power summation node, then the phase of the wave components in each mode is preserved after mixing. The optical mixer includes a directional coupler to combine a reference optical signal acting as a local oscillator (LO) (with an optical frequency of ω_L) and the input wave, as well as a photodiode pair (e.g., made of germanium in a silicon photonics process) to convert the optical wave into an electrical current. Moreover, the phase shifters in the LO path, symbolically shown as ϕ_1 and ϕ_2, allow for controlling the output phase of the mixer. As shown in [7], [12], the output current of an optoelectronic mixer is proportional to the signal strength at the beat frequency, $\omega_b = |\omega_0 - \omega_L|$, namely,

$$I_{out} \propto \cos((\omega_0 - \omega_L)t + \phi_0 - \phi_L), \tag{14}$$

where R is the responsivity of the photo-diode and ω_0 and ω_L are illumination and LO wave frequencies, respectively.

While the modes are assumed independent in the system-level representation of Fig. 17, they share the same spatial region and have considerable overlap in the multi-mode pillar antenna discussed in the previous section. To increase the separation between the modes, a pair of coupled pillars can be used as an antenna, Fig. 18. This system consists of several pillars that are arranged in close vicinity of each other, where light can couple from one to another. There are several supported modes in this structure and each mode has a different reception pattern. Fig. 18 shows two 0.6 μm by 0.6 μm coupled pillars with 0.2 μm gap between them are used as a unit cell of an infinite array with

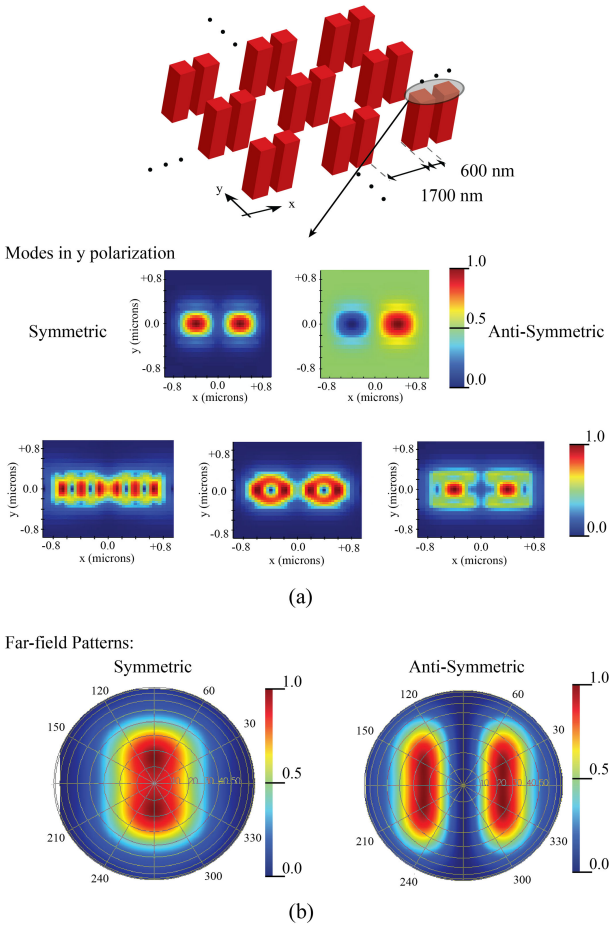

Fig. 18. (a) coupled pillar structure with supported modes, (b) far-field pattern of symmetric and anti-symmetric modes.

3 μnm cell pitch. This structure supports two main modes, the symmetric and anti-symmetric modes (Fig. 18). The symmetric mode refers to a situation where the excited waves in both pillars have the same phase and amplitude, also known as the common mode. On the other hand, the anti-symmetric mode (a.k.a. the differential mode), corresponds to the excitation in which the phases of the wave in the pillars are 180° out of phase. The other supported modes by the coupled pillar antenna are shown in Fig. 18(a). These modes have effective indices near silicon which means they are mostly confined inside the silicon pillars. Also, polarization of these modes are close to the direction of y axis. For an incident plane wave with an electric field polarization in y axis direction, E_y, only symmetric and anti-symmetric modes have the exact same polarization matching. The far-field radiation patterns of these two modes are shown in Fig. 18(b) showing that they collectively cover a larger FOV than individually. Therefore, the light coming from different angles couples into different modes of the antenna structure.

To understand the behavior of this structure, we decomposed the electric field excitation inside the silicon pillars into the supported modes for two exemplary cases: a plane wave with E_y polarization impinging at 0° and a plane wave with E_y polarization arriving at 20°. As shown in Fig. 19(a), for the first scenario, most of the power couples to the symmetric mode (mode 1). As the illumination angle increases, some of the power shifts

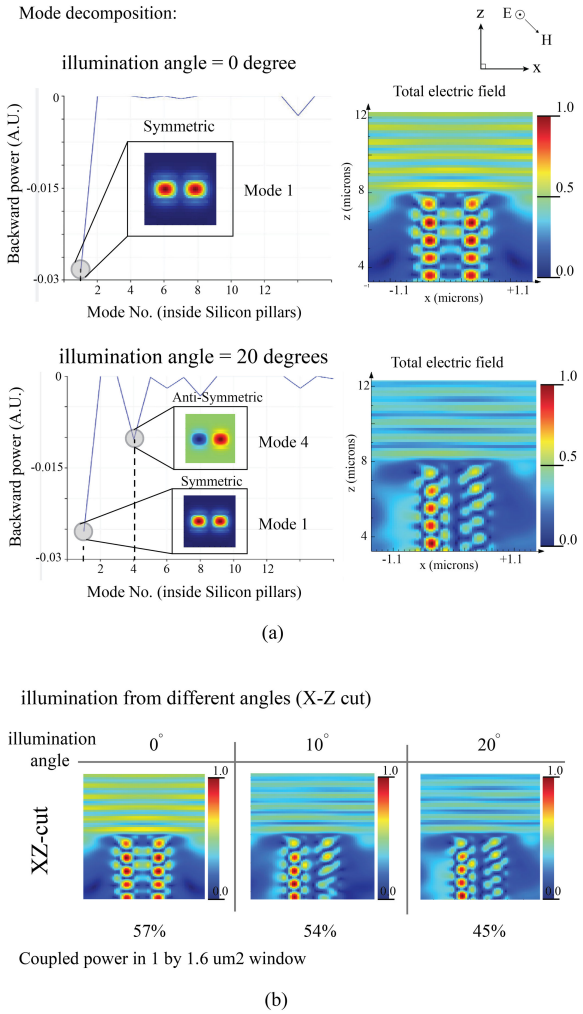

Fig. 19. (a) Mode expansion simulation at different illumination angles. (b) Electric field magnitude in X-Z cut vs. different illumination angles.

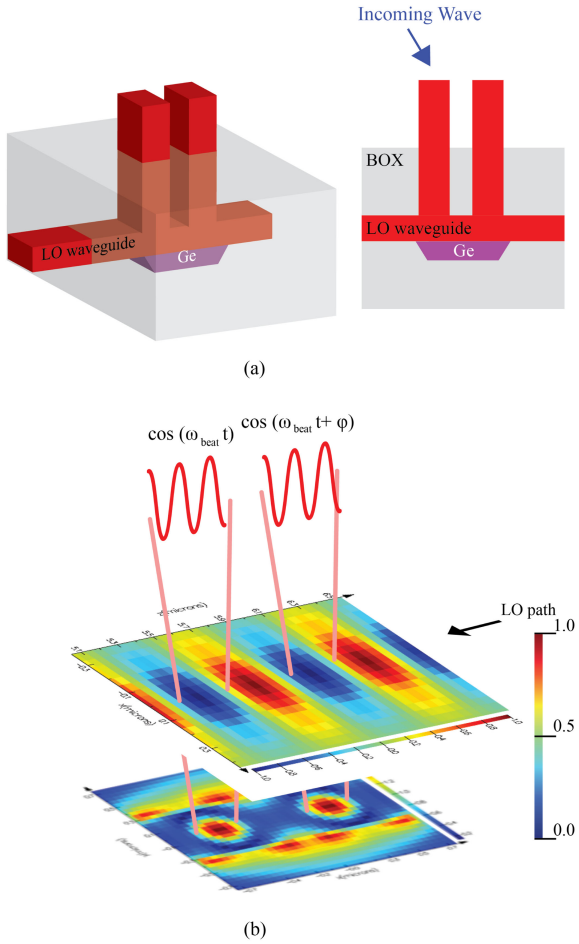

Fig. 20. (a) Heterodyne detection combined with two-pillar structure. (b) simulated electric field strength at zero-angle illumination. Fields maximize under the pillars and the relative phase between LO wave and the illumination has to be the same at the hot spots.

to the anti-symmetric mode (mode 4). Since the polarization only matches with these two modes, the coupled power to the other supported modes is negligible. Also, part of the power is coupled to the extra supported modes associated with the array structure which are mainly concentrated in the inter-pillar space with effective indices around 1. The properties of these modes can be manipulated by covering the pillars with silicon oxide (Fig. 20). Fig. 19(b) illustrate the total electric field underneath the silicon pillars for the two illuminations at 0° and 20°.

Since for illumination at 0° the optical power mostly couples into the symmetric mode, light travels through both pillars. Fig. 19(b) shows the electric field magnitude for this case in the X-Z cut. As the angle of illumination increases, both symmetric and anti-symmetric modes are excited. Therefore, the total electric field is the superposition of these two modes. Due to the phase distribution of the two mode profiles, superposition results in having optical power mostly in one pillar rather than both of them, as seen in Fig. 19(b), while the effective aperture of the antenna is maintained. According to the simulation results, the 3dB FOV of this structure is more than 50°.

The discussed heterodyne detection scheme can be used with this pillar array configuration by routing a waveguide carrying the LO signal underneath the pillar pairs as shown in Fig. 20 (a). Here, a slab of germanium operates as the mixer and the combiner, shown with building blocks in Fig. 17. The mixing is achieved through the beating between the LO and the coupled incident light followed by the absorption within the germanium slab. The absorption of light generates temporally varying electron-hole pairs with phases determined by the LO and input wave phases at each point. The electrons and holes are then swept to the two ports of the photodetector and the total output current is the coherent sum of all these regional currents. As mentioned, for different illumination angles, the superposition of symmetric and anti-symmetric modes controls the power balance in the two pillars, Fig. 19(a) (b). This means that there are two main hot spots underneath each pillar within the germanium slab where most of the mixing and combining occurs. These two spots are not in-phase and there is a phase difference for the electromagnetic field present at these two places. Therefore, to achieve a coherent sum and combine the powers of the two modes, as the LO signal propagates in the structure, it should experience a phase shift equal to the phase difference of the two hot spots which yields in-phase beat components. This is done by adjusting the physical dimensions of the structure and controlling the propagation constant of the waves. Consequently,

the LO waveguide, its wavelength, and the gap between two pillars as well as their sizes must be designed in a way that two beat-frequency signals have the same phases (Fig. 20) and add constructively. To combine the LO wave with the received wave through pillars, the polarization of the electric fields inside the pillars and the LO waveguide have to be aligned (direction of y axis in this case). Here, the electric fields are combined inside the waveguide and a directional coupler used in optoelectronic mixer [7] can be eliminated. The germanium slab is added underneath the LO waveguide to convert the combined electric fields into electrical current. Connections to the germanium can be made by having doped p- and n-type regions next to the LO waveguide forming a PIN diode.

VII. Conclusion

In this paper, we studied the fundamental limits of antenna design for photonic transmitter and receiver systems and proposed architectures for designing high-performance antennas. An approximated upper bound for radiation efficiency of a transmitter antenna in standard single-layer silicon photonics processes is derived based on which architectures for improving the radiated power fraction and reducing the stray light are demonstrated. For the receiver antenna, maximizing the collection efficiency while maintaining the FOV of the receiver is the desired design target due to the typically weak received signal levels. However, the strong relationship between the antenna characteristics in the transmit and receive modes introduce trade-offs in the design space of conventional antennas. Via an idealized model, the trade-offs are quantified and novel architectures for designing high-performance antennas beyond these limitations are demonstrated. Finally, a photonic coherent receiver achieving more than 95% collection efficiency and 170° of FOV utilizing a multi-mode dense pillar antenna array is demonstrated.

References

[1] J. K. Doylend *et al.*, "Two-dimensional free-space beam steering with an optical phased array on silicon-on-insulator," *Opt. Express*, vol. 19, no. 22, pp. 21 595–21 604, Oct. 2011.

[2] K. V. Acoleyen *et al.*, "Off-chip beam steering with a one-dimensional optical phased array on silicon-on-insulator," *Opt. Lett.*, vol. 34, no. 9, pp. 1477–1479, May 2009.

[3] F. Ashtiani and F. Aflatouni, "N × N optical phased array with 2N phase shifters," *Opt. Express*, vol. 27, no. 19, pp. 27 183–27 190, Sep. 2019.

[4] R. Fatemi, A. Khachaturian, and A. Hajimiri, "A nonuniform sparse 2-D large-FOV optical phased array with a low-power PWM drive," *IEEE J. Solid-State Circuits*, vol. 54, no. 5, pp. 1200–1215, May 2019.

[5] Q. Wang *et al.*, "Dual-layer waveguide grating antenna with high directionality for optical phased arrays," *Appl. Opt.*, vol. 58, no. 21, pp. 5807–5811, Jul. 2019.

[6] Y. Wang *et al.*, "High resolution grating antennas for beam steering on the imos platform," in *Proc. Asia Commun. and Photon. Conf.*, 2019, Paper M4B.5.

[7] R. Fatemi, B. Abiri, A. Khachaturian, and A. Hajimiri, "High sensitivity active flat optics optical phased array receiver with a two-dimensional aperture," *Opt. Express*, vol. 26, no. 23, pp. 29 983–29 999, Nov. 2018.

[8] P. F. Wang *et al.*, "Improving the performance of optical antenna for optical phased arrays through high-contrast grating structure on SOI substrate," *Opt. Express*, vol. 27, no. 3, pp. 2703–2712, Feb. 2019.

[9] R. Fatemi, A. Khachaturian, and A. Hajimiri, "A low power PWM optical phased array transmitter with 16° field-of-view and 0.8° beamwidth," in *Proc. IEEE Radio Frequency Integr. Circuits Symp.*, 2018, pp. 28–31.

[10] M. Raval, C. V. Poulton, and M. R. Watts, "Unidirectional waveguide grating antennas with uniform emission for optical phased arrays," *Opt. Lett.*, vol. 42, no. 13, pp. 2563–2566, Jul. 2017.

[11] R. Fatemi, A. Khachaturian, and A. Hajimiri, "Scalable optical phased array with sparse 2D aperture," in *Proc. Conf. Lasers and Electro-Opt.*, 2018, Paper STu4B.6.

[12] B. Abiri, R. Fatemi, and A. Hajimiri, "A 1-D heterodyne lens-free optical phased array camera with reference phase shifting," *IEEE Photon. J.*, vol. 10, no. 5, pp. 1–12, Oct. 2018.

[13] F. Aflatouni, B. Abiri, A. Rekhi, and A. Hajimiri, "Nanophotonic coherent imager," *Opt. Express*, vol. 23, no. 4, pp. 5117–5125, Feb. 2015.

[14] C. V. Poulton *et al.*, "Long-range LiDAR and free-space data communication with high-performance optical phased arrays," *IEEE J. Sel. Topics Quantum Electron.*, vol. 25, no. 5, pp. 1–8, Sep. 2019.

[15] F. Aflatouni, B. Abiri, A. Rekhi, and A. Hajimiri, "Nanophotonic projection system," *Opt. Express*, vol. 23, no. 16, pp. 21 012–21 022, 2015.

[16] R. Fatemi, B. Abiri, and A. Hajimiri, "An 8×8 heterodyne lens-less OPA camera," in *Proc. Conf. Lasers Electro-Opt.*, 2017, Paper JW2A.9.

[17] A. White, P. Khial, F. Salehi, B. Hassibi, and A. Hajimiri, "A silicon photonics computational lensless active-flat-optics imaging system," *Scientific Rep.*, vol. 10, no. 1, 2020, Art. no. 1689.

[18] J. L. Pita, I. Aldaya, P. Dainese, H. E. Hernandez-Figueroa, and L. H. Gabrielli, "Design of a compact CMOS-compatible photonic antenna by topological optimization," *Opt. Express*, vol. 26, no. 3, pp. 2435–2442, Feb. 2018.

[19] C. V. Poulton *et al.*, "Large-scale silicon nitride nanophotonic phased arrays at infrared and visible wavelengths," *Opt. Lett.*, vol. 42, no. 1, pp. 21–24, Jan. 2017.

[20] R. Fatemi, B. Abiri, and A. Hajimiri, "A one-dimensional heterodyne lens-free OPA camera," in *Proc. Conf. Lasers and Electro-Opt.*, 2016, Paper STu3G.3.

[21] J. Kraus and R. Marhefka, *Antennas for all applications*, (McGraw-Hill series in electrical engineering Series). New York, NY, USA: McGraw-Hill, 2002. [Online]. Available: https://books.google.com/books?id=NRxTAAAAMAAJ

[22] D. Pozar, *Microwave Engineering, 4th ed.*. Hoboken, NJ, USA: Wiley, 2011. [Online]. Available: https://books.google.com/books?id=JegbAAAAQBAJ

[23] D. Cheng, *Field and Wave Electromagnetics*, (Addison-Wesley series in electrical engineering Series). Reading, MA, USA: Addison-Wesley Publishing Company, 1989. [Online]. Available: https://books.google.com/books?id=KL_vAAAAMAAJ

[24] J. Goodman, *Introduction to Fourier Optics*, (McGraw-Hill physical and quantum electronics series Series). San Francisco, CA, USA: Freeman, 2005. [Online]. Available: https://books.google.com/books?id=ow5xs_Rtt9AC

[25] N. V. Sapra *et al.*, "Inverse design and demonstration of broadband grating couplers," *IEEE J. Sel. Topics Quantum Electron.*, vol. 25, no. 3, pp. 1–7, May/Jun. 2019.

[26] N. M. Andrade *et al.*, "Inverse design optimization for efficient coupling of an electrically injected optical antenna-led to a single-mode waveguide," *Opt. Express*, vol. 27, no. 14, pp. 19 802–19 814, Jul. 2019.

[27] A. Michaels and E. Yablonovitch, "Inverse design of near unity efficiency perfectly vertical grating couplers," *Opt. Express*, vol. 26, no. 4, pp. 4766–4779, Feb. 2018.

[28] Y. Luo *et al.*, "Low-loss two-dimensional silicon photonic grating coupler with a backside metal mirror," *Opt. Lett.*, vol. 43, no. 3, pp. 474–477, Feb. 2018.

[29] W. Bogaerts *et al.*, "A polarization-diversity wavelength duplexer circuit in silicon-on-insulator photonic wires," *Opt. Express*, vol. 15, no. 4, pp. 1567–1578, Feb. 2007.

[30] T. Watanabe, Y. Fedoryshyn, and J. Leuthold, "2-D grating couplers for vertical fiber coupling in two polarizations," *IEEE Photon. J.*, vol. 11, no. 4, pp. 1–9, Aug. 2019.

[31] J. Mautz and R. Harrington, "Modal analysis of loaded n-port scatterers," *IEEE Trans. Antennas and Propag.*, vol. 21, no. 2, pp. 188–199, Mar. 1973.

[32] R. Harrington and J. Mautz, "Pattern synthesis for loaded n-port scatterers," *IEEE Trans. Antennas Propag.*, vol. 22, no. 2, pp. 184–190, Mar. 1974.

[33] R. G. Vaughan, "Two-port higher mode circular microstrip antennas," *IEEE Trans. Antennas and Propag.*, vol. 36, no. 3, pp. 309–321, Mar. 1988.

[34] C. Waldschmidt and W. Wiesbeck, "Compact wide-band multimode antennas for MIMO and diversity," *IEEE Trans. Antennas Propag.*, vol. 52, no. 8, pp. 1963–1969, Aug. 2004.

[35] T. Svantesson, "Correlation and channel capacity of MIMO systems employing multimode antennas," *IEEE Trans. Veh. Technol.*, vol. 51, no. 6, pp. 1304–1312, Nov. 2002.

[36] M. Cabedo-Fabres, E. Antonino-Daviu, A. Valero-Nogueira, and M. F. Bataller, "The theory of characteristic modes revisited: A contribution to the design of antennas for modern applications," *IEEE Antennas Propag. Mag.*, vol. 49, no. 5, pp. 52–68, Oct. 2007.
[37] R. Harrington and J. Mautz, "Theory of characteristic modes for conducting bodies," *IEEE Trans. Antennas Propag.*, vol. 19, no. 5, pp. 622–628, Sep. 1971.
[38] R. J. Garbacz, "Modal expansions for resonance scattering phenomena," *Proc. IEEE*, vol. 53, no. 8, pp. 856–864, Aug. 1965.
[39] W. Hong *et al.*, "Multibeam antenna technologies for 5G wireless communications," *IEEE Trans. Antennas Propag.*, vol. 65, no. 12, pp. 6231–6249, Dec. 2017.
[40] P. Velha *et al.*, "Wide-band polarization controller for Si photonic integrated circuits," *Opt. Lett.*, vol. 41, no. 24, pp. 5656–5659, Dec. 2016.
[41] Y. Xu, J. Wang, J. Xiao, and X. Sun, "Design of a compact silicon-based slot-waveguide crossing," *Appl. Opt.*, vol. 52, no. 16, pp. 3737–3744, 2013.
[42] L. F. Frellsen, Y. Ding, O. Sigmund, and L. H. Frandsen, "Topology optimized mode multiplexing in silicon-on-insulator photonic wire waveguides," *Opt. Express*, vol. 24, no. 15, pp. 16 866–16 873, 2016.
[43] J. Lu and J. Vučković, "Nanophotonic computational design," *Opt. Express*, vol. 21, no. 11, pp. 13 351–13 367, 2013.
[44] D. Dai and H. Wu, "Realization of a compact polarization splitter-rotator on silicon," *Opt. Lett.*, vol. 41, no. 10, pp. 2346–2349, May 2016.
[45] W. D. Sacher, T. Barwicz, B. J. F. Taylor, and J. K. S. Poon, "Polarization rotator-splitters in standard active silicon photonics platforms," *Opt. Express*, vol. 22, no. 4, pp. 3777–3786, Feb. 2014.
[46] Z. Lu *et al.*, "Silicon photonic polarization beamsplitter and rotator for on-chip polarization control," in *Proc. IEEE 13th Int. Conf. Group IV Photon. (GFP)*, 2016, pp. 70–71.
[47] M. Ma *et al.* "Sub-wavelength grating-assisted polarization splitter-rotators for silicon-on-insulator platforms," *Opt. Express*, vol. 27, no. 13, pp. 17 581–17 591, Jun. 2019.
[48] W. White, "Pattern limitations in multiple-beam antennas," *IRE Trans. Antennas Propag.*, vol. 10, no. 4, pp. 430–436, 1962.
[49] C. J. Chang-Hasnain and W. Yang, "High-contrast gratings for integrated optoelectronics," *Adv. Opt. Photon.*, vol. 4, no. 3, pp. 379–440, Sep. 2012.

Reza Fatemi (Student Member, IEEE) received the B.S. degree in electrical engineering from K. N. Toosi University of Technology, Tehran, Iran, in 2011, the M.S. degree in electrical engineering from the Sharif University of Technology (SUT), Tehran, in 2013, and the Ph.D. degree in electrical engineering from the California Institute of Technology (Caltech), Pasadena, CA, USA, in 2020. Mr. Fateni was awarded the Oringer and Kilgore Fellowship in 2014 and the Analog Devices Outstanding Student Designer Award in 2015. His research interests are in silicon photonics and high-speed integrated circuit design.

Parham P. Khial (Student Member, IEEE) was born in Tehran, Iran, in 1993. He received the B.S. degree in electrical engineering from the Sharif University of Technology, Tehran, in 2015, and the M.S. degree in electrical engineering in 2016, from the California Institute of Technology (Caltech), Pasadena, CA, USA, where he is currently working toward the Ph.D. degree in electrical engineering under the supervision of Prof. Hajimiri. His current research interests include millimeter-wave and radio frequency integrated circuits for biomedical and communications applications, and silicon photonics platforms for the next generation of optical sensors.

Mr. Khial was a recipient of the Gold Medal winner of the National Astronomy Olympiad in Iran, in 2010, the Bronze and Silver Medal winner of the 5th International Olympiad on Astronomy and Astrophysics (5th IOAA) in Poland, 2011, and the Analog Devices Outstanding Student Designer Award in 2016.

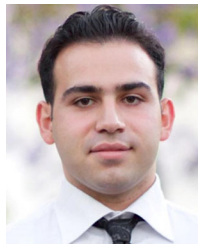

Aroutin Khachaturian (Student Member, IEEE) received the B.S. and M.S. degrees in electrical engineering from the California Institute of Technology (Caltech), Pasadena, CA, USA, in 2013 and 2014, respectively. He is currently working toward the Ph.D. degree in electrical engineering at Caltech. Mr. Khachaturian was a recipient of the Killgore Fellowship and the Analog Devices, Inc. Outstanding Student Designer Award in 2013. His research interests are in the design of integrated electro-optics systems for high-speed optical interconnects and photonic beamforming techniques for communications, imaging, and remote sensing.

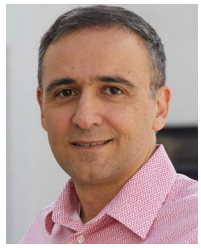

Ali Hajimiri (Fellow, IEEE) received the B.S. degree in electronics engineering from the Sharif University of Technology, Tehran, Iran, in 1994, and the M.S. and Ph.D. degrees in electrical engineering from Stanford University, Stanford, CA, USA, in 1996 and 1998, respectively.

He has been with Philips Semiconductors, where he worked on a BiCMOS chipset for GSM and cellular units from 1993 to 1994. In 1995, he was with Sun Microsystems, Santa Clara, CA, USA, working on the UltraSPARC microprocessors cache RAM design methodology. During the summer of 1997, he was with Lucent Technologies (Bell Labs), Murray Hill, NJ, USA, where he investigated low phase noise integrated oscillators. In 1998, he joined the faculty of the California Institute of Technology, Pasadena, CA, USA, where he is the Bren Professor of Electrical Engineering and Medical Engineering and the Director of the Microelectronics Laboratory and Codirector of Space Solar Power Project. His research interests are in high-speed and high-frequency integrated circuits for applications in sensors, photonics, biomedical devices, and communication systems.

Dr. Hajimiri is a Fellow of National Academy of Inventors (NAI). He was selected to the TR35 top innovator's list. He has served as a Distinguished Lecturer of the IEEE Solid-State and Microwave Societies. He is the author of *Analog: Inexact Science, Vibrant Art* (2020, Early Draft) a book on fundamental principles of analog circuit design and *The Design of Low Noise Oscillators* (Boston, MA: Springer). He has authored and coauthored more than 250 refereed journal and conference technical articles and has been granted more than 120 US patents with many more pending applications. He won the Feynman Prize for Excellence in Teaching, Caltech's most prestigious teaching honor, as well as Caltech's Graduate Students Council Teaching and Mentoring award and the Associated Students of Caltech Undergraduate Excellence in Teaching Award. He was the gold medal winner of the National Physics Competition and the bronze medal winner of the 21st International Physics Olympiad, Groningen, Netherlands. He was recognized as one of the top-10 contributors to ISSCC. He was a corecipient of the IEEE Journal of Solid-State Circuits Best Paper Award of 2004, the International Solid-State Circuits Conference (ISSCC) Jack Kilby Outstanding Paper Award, a corecipient of RFIC best paper award, a two-time co-recipient of CICC best paper award, and a three-time winner of the IBM faculty partnership award, as well as National Science Foundation CAREER award and Okawa Foundation award. In 2002, he cofounded Axiom Microdevices Inc., Irvine, CA, USA, whose fully integrated CMOS PA has shipped around 400 000 000 units, and was acquired by Skyworks Inc., Irvine, CA, USA, in 2009. He has served on the Technical Program Committee of the *International Solid-State Circuits Conference (ISSCC)*, as an Associate Editor for the *IEEE Journal of Solid-State Circuits (JSSC)* and for IEEE TRANSACTIONS ON CIRCUITS AND SYSTEMS (TCAS): PART-II, as a member of the Technical Program Committees of the *International Conference on Computer Aided Design (ICCAD)*, Guest Editor of the IEEE TRANSACTIONS ON MICROWAVE THEORY AND TECHNIQUES, and Guest Editorial Board of Transactions of Institute of Electronics, Information and Communication Engineers of Japan (IEICE).